AGU ADVANCING EARTH AND SPACE SCIENCES

Earth and Space Science

RESEARCH ARTICLE
10.1029/2024EA004098

Special Collection:
Surface Topography and Vegetation: Science, Measurements, and Technologies

Empirical Quantification of Topobathymetric Lidar System Resolution Using Modulation Transfer Function

K. W. Sacca[1] **and J. P. Thayer**[1]

[1]Active Remote Sensing Laboratory (ARSENL), Ann and H.J. Smead Department of Aerospace Engineering Sciences, University of Colorado Boulder, Boulder, CO, USA

Abstract Topobathymetric scanning lidar deployed on unmanned aircraft systems is a powerful tool for high-resolution mapping of the dynamic interface between topography and bathymetry. However, standardized methods for empirical resolution validation have not been widely adopted across lidar applications. While theoretical models of idealized lidar sampling resolution can be used to describe topographical resolution, misrepresented or unknown behaviors in an instrument, platform, or environment can degrade expected performance or introduce georeferencing inaccuracies. Furthermore, bathymetric resolution is strongly dependent on water surface and column conditions. Thus, only empirical methods for evaluating resolution will provide reliable estimates for both topographic and bathymetric surveys. Presented is an extension of standard modulation transfer function (MTF) methods used by passive imaging systems applied to high-resolution scanning lidar. Compact retroreflectors characterized as point and line sources are employed to empirically assess effective lidar system resolution through MTF analysis in topographic and bathymetric scenes. These targets enable MTF analyses using height measurements without reliance on intensity data, promoting widespread applicability among lidar systems. Empirical MTFs calculated using these targets are compared against theory-derived counterparts as empirical measurements elucidate influences by elements that are unknown or difficult to model. Simulated point cloud data were incorporated into theoretical MTF descriptions to better represent empirically-derived topographic MTFs, revealing mirror pointing uncertainties in the across-track axis. Similarly, theoretical bathymetric MTFs augmented with simulated, subaqueous data enabled water surface slope estimation using empirical measurements of submerged retroreflector targets, where rough water surfaces strongly influenced beam steering and the corresponding point spread MTFs.

Key Points:

- Standard imaging modulation transfer function (MTF) methods are applied to topobathymetric lidar using compact retroreflector targets to quantify effective resolution
- Height-based MTFs are leveraged for lidar resolution analysis without intensity data and are shown to have reliable theoretical descriptions
- Empirical lidar MTFs quantified unknown instrument pointing and water surface steering errors that improved theoretical estimates of MTF

Correspondence to:
K. W. Sacca,
Kevin.Sacca@colorado.edu

Citation:
Sacca, K. W., & Thayer, J. P. (2025). Empirical quantification of topobathymetric lidar system resolution using modulation transfer function. *Earth and Space Science*, *12*, e2024EA004098. https://doi.org/10.1029/2024EA004098

Received 14 NOV 2024
Accepted 9 MAR 2025

Author Contributions:
Conceptualization: K. W. Sacca
Data curation: K. W. Sacca
Formal analysis: K. W. Sacca, J. P. Thayer
Funding acquisition: K. W. Sacca, J. P. Thayer
Investigation: K. W. Sacca, J. P. Thayer
Methodology: K. W. Sacca
Project administration: J. P. Thayer
Resources: K. W. Sacca, J. P. Thayer
Software: K. W. Sacca
Supervision: J. P. Thayer
Validation: K. W. Sacca, J. P. Thayer

1. Introduction

Scanning topobathy lidar instrumentation operating from unmanned aircraft system (UAS) platforms are capable of topographic and bathymetric mapping at very high resolutions (Mandlburger et al., 2020; Thayer et al., 2022). Applications that demand high resolutions from topobathymetric lidar, such as object detection and classification, biomass estimation, change detection, hydrographic surveying, etc., should employ strategies that routinely validate resolution performance as instrumental or environmental factors can have a significant impact on effective instrument system resolution (Donnellan et al., 2021; Goulden & Hopkinson, 2010; Hancock et al., 2019; International Hydrographic Organization, 2022; Kellner et al., 2019; Mandlburger, 2022; National Oceanic and Atmospheric Administration, 2020). Resolution is a performance metric without a standardized definition across applications. The *resolution* of an instrument is defined here as the ability to discern two point sources from measurements and is distinguished from *sampling*, which describes the density of measurements. Point density and point spacing metrics are commonly used to quantify lidar resolution, however, these metrics do not capture the inherent spatial spread of signal through an optical system that impacts measurement discernibility. This important distinction serves to convey that resolution is dependent on the sampling and signal contrast of measurements.

Passive camera imaging in UAS-, aircraft-, and spacecraft-based remote sensing applications regularly leverage standardized methods for empirically evaluating resolution during operations (Fiete, 1999; Reichenbach et al., 1991; Williams & Burns, 2001). Since the 1980s and persisting today, ground targets used in resolution estimation have been designed for modulation transfer function (MTF) analysis methods, which relate signal contrast to spatial resolution and quantify resolution performance across an instrument's complete range of resolvable spatial frequencies (Eon et al., 2024; Markham, 1985; Storey, 2001). MTF methods are not limited by a

Visualization: K. W. Sacca
Writing – original draft: K. W. Sacca
Writing – review & editing: K. W. Sacca, J. P. Thayer

particular instrument, platform, resolution range, or environment which makes MTF a suitable figure of merit for standardized resolution analysis.

Across the field of lidar, there is no unifying standard method for empirical resolution analysis. It is common to use fundamental instrument models to estimate resolvability theoretically (Lichti, 2004; Ullrich & Pfennigbauer, 2016), or utilize vicarious calibration targets in large-scale surveys, such as from aircraft or spacecraft platforms (Collin et al., 2008; Kuester et al., 2010; McCarthy et al., 2022). Hancock et al. (2019) have demonstrated high fidelity lidar measurement and noise models to validate empirical data, but the model is specific to waveform lidar and does not consider MTF. This study aims to apply MTF to any lidar instrument. MTF has not yet been widely practiced or adopted in the field of lidar, but previous work has proved MTF can be applied to both intensity and height measurements of lidar allowing for multimodal resolution performance estimation (Albota et al., 2017; Goesele et al., 2003; Miles et al., 2002, 2010; Stevens et al., 2011). However, MTF has a variety of implementations and specific methods for geoscience applications that have not been fully demonstrated to satisfy the needs of all lidar systems.

Shallow water bathymetry is a unique application area for scanning lidar due to the higher depth-penetration capability of pulsed lasers compared to sunlight for passive imaging systems (Forfinski-Sarkozi & Parrish, 2019; Mandlburger, 2022; Parrish et al., 2013; Schwarz et al., 2019; Thayer et al., 2022). Proposed missions like NASA's Surface Topography and Vegetation (STV) (Donnellan et al., 2024) with targeted observables demanding high resolutions, such as shallow-water bathymetry, will require empirical means to validate effective resolution to ensure scientific objectives are met. Shallow waters are areas of great interest for frequent mapping but are also very challenging areas to acquire accurate georeferenced data due to dynamic water surface and column effects (Parrish et al., 2019). Empirical measurements of MTF represent the entire imaging chain, including environmental factors, making it uniquely suited to characterizing the effective resolution of an instrument in the presence of unknown influences (Boreman, 2001; Schott, 2007).

Presented here are empirical methods for MTF-based resolution performance analysis of a UAS-based topobathy lidar instrument. Section 2 describes the fundamental relationships between MTF and point spread function (PSF), previous applications of MTF to lidar, and provides a description of the UAS-based lidar instrument used for empirical results. Section 3 covers the theoretical descriptions of MTF using fundamental definitions, an overview of the empirical methods employed here for lidar point cloud analysis, and a description of the retroreflector targets designed for use in topobathymetric surveys to assess resolution and satisfy needs of groups like NASA's STV community. Empirical application of standard MTF methods to lidar data are presented in Section 4, alongside several theoretical models of MTF that support empirical results for topographic and bathymetric environments. Section 5 summarizes and highlights conclusions and impacts of MTF on topobathymetric lidar applications.

2. Background

Modulation, M, (also known as contrast) is the ratio of the bias level and the amplitude of sinusoidal or square wave signals of a particular frequency, ξ, in object and image space and is expressed as (Boreman, 2001):

$$M(\xi) = \frac{I_{\max} - I_{\min}}{I_{\max} + I_{\min}} \tag{1}$$

Modulation transfer is a metric that quantifies an instrument's ability to reproduce real spatial frequencies and associated contrast observed in an imaged scene, defined as:

$$MTF(\xi) = \frac{M_{\text{image}}}{M_{\text{object}}} \tag{2}$$

where $MTF(\xi)$ is the MTF at frequency ξ and is defined as the ratio of recorded image modulation to the true object modulation where MTF = 1 signifies perfect image reproduction of a feature (Boreman, 2001; Schott, 2007). However, due to realistic sampling limitations, imaging instruments impart a minimum spatial spread to signals that bounds the range of reproducible frequencies. The "instrument system MTF" encompasses all contributing sources of signal spread on a measurement, such as noise, platform, and environmental factors.

Boreman (2001) is one of the most thorough references containing theoretical derivations of MTF, imaging relationships between MTF and PSF, line spread function (LSF), and edge spread function (ESF), and the cascading nature of system MTF into individual component MTFs. Interested readers are encouraged to seek that source for more detailed descriptions of MTF. The important aspect of MTF that has been leveraged extensively in remote sensing image applications is that PSF and MTF are related via the Fourier transform. Therefore, empirical PSF measurements can be used to evaluate MTF. LSF and ESF also have similar definitions that relate to MTF that translate to physical measurements of line and edge sources.

Direct measurements of modulation, or contrast, using Equation 1 with samples of square-wave targets geometrically arranged into specific frequencies produces a function similar to MTF known as the contrast transfer function (CTF) (Boreman, 2001; Boreman & Yang, 1995). Contrast transfer function is discretely sampled using pairs of these targets while MTF is a continuous function defined by a sinusoid response (Boreman & Yang, 1995; Coltman, 1954). Previous applications of empirical MTF methods to an airborne, scanning, topographic lidar mainly involved discretized CTF measurements and an approximation of MTF using fundamental relationships between square and sinusoid functions (Miles et al., 2010; Stevens et al., 2011). Point, line, and edge spread measurements of compact targets produce direct and continuous estimates of MTF without the need for large square wave targets, making it an ideal technique for straightforward integration into geospatial lidar survey operations (Boreman & Yang, 1995; Reichenbach et al., 1991). It is this aspect of MTF analysis that is applied in this study. For an ideal image, $f(x,y)$, and an instrument response function (IRF), $h(x,y)$, the instrument image function can be written as (Boreman, 2001):

$$g(x,y) = f(x,y) * h(x,y) \tag{3}$$

For point source targets, $f(x,y)$ can be written as a delta function, $\delta(x,y)$, such that the instrument image function convolved with the delta algebraically describes how to empirically measure the optical transfer function (OTF). The IRF is the convolution of each component impulse response, or PSF, present in the system. Through the Fourier transform, we can represent Equation 3 in the frequency domain for the point source case with N component transfer functions as (Boreman, 2001):

$$G(\xi,\eta) = \delta(\xi,\eta) \times H(\xi,\eta) = \delta(\xi,\eta) \times H_1(\xi,\eta) \times H_2(\xi,\eta) \times \cdots \times H_N(\xi,\eta) \tag{4}$$

where $H(\xi,\eta)$ is the overall OTF and $G(\xi,\eta)$ represents the empirical measurement of the OTF using a point source target. The OTF can contain any number of component transfer functions, corresponding to any optical element, sampling architecture, environmental influences, etc. That describe the end-to-end imaging system. We can define MTF as (Boreman, 2001):

$$MTF \equiv |H(\xi,\eta)| \tag{5}$$

where the real component, or magnitude, of the OTF is defined as MTF, and this theoretical description of MTF is leveraged to obtain empirical measurements of MTF in lidar.

Welsh and Gardner (1989) describe the practical relationships between PSF and OTF that determine resolution limitations fundamental to MTF theory, but does not cover MTF or the effective PSF obtained through multiple single-detector measurements which are relevant to scanning lidar systems. Dolin (2013) presents a theoretical framework for measuring the MTF of a water surface for bathymetric lidar applications but requires auxiliary imaging instrumentation that is not relevant across the range of applications utilizing scanning lidar. A high priority of this work is to provide a universally relevant approach to lidar system MTF that can be obtained empirically.

Miles et al. (2010) demonstrated empirical, intensity-based, PSF-derived MTF with aerial topographic lidar. However, among the two methods implemented, one produced PSF estimates that mismatched observations and the other relied on the removal of background noise. This can introduce artificial features or contrast in the PSF resulting in an MTF that is not fully representative of the system. Lichti (2004) demonstrated the comparison in resolution performance between scanning topographic lidar instrumentation using MTF but only through theoretical models of fundamental sampling behaviors that do not capture noise or extrinsic contributions to effective

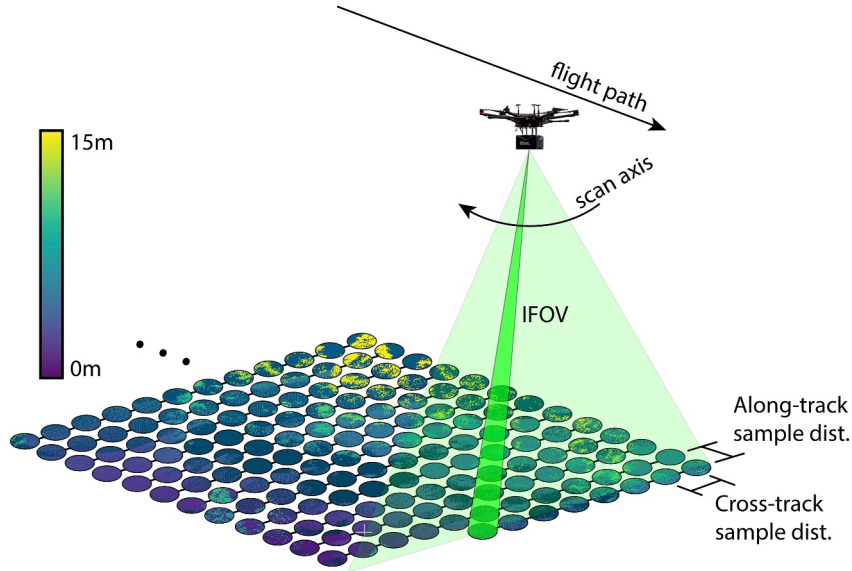

Figure 1. Example sampling diagram for a scanning topobathy lidar instrument illustrating along-track and across-track sample distances relative to the flight and scan axes. Here, the scan axis is orthogonal to the flight path and the color scale indicates bathymetry depths.

resolution. While theoretical descriptions of MTF can address high-level instrument trade spaces, robust performance estimates demand empirical methods to validate salient instrument specifications, as will be shown in Section 4. Goesele et al. (2003) demonstrated an example of empirical, height-based MTF measurements using knife edge targets inspired by imaging standards, but did not demonstrate the translation of their method to real-world lidar applications or relate empirical MTFs to component MTFs that can be derived theoretically.

The empirical methods presented here utilize point and line source targets to independently evaluate MTF using standardized image methods adapted to lidar and are supported by theoretical descriptions of MTF. The incorporation of lidar height-based MTF methods into geospatial applications could have far reaching and lasting impact on how lidar data is collected, validated, and standardized.

The instrument used for empirical demonstrations is a prototype UAS-based scanning topobathy lidar system from Orion Space Solutions (2025) (formerly LiteWave Technologies) that produces scan patterns represented by the illustration in Figure 1. This Geiger-mode lidar operates with a 532 nm green laser pulsed at 20 kHz and a scanning mechanism operating at 70 Hz that produces a linear cross-track scan pattern spanning ±15° through nadir. All data used to demonstrate these MTF analysis methods were received from Orion and are georeferenced, GPS-corrected, and boresight-calibrated 3-D point clouds. The point cloud data contains 3-D XYZ coordinates and measurement timestamps. The topographic MTF analyses are performed on data collected across several surveys and different locations. The bathymetric MTF analyses are performed on data collected from a near-shore area of the Gulf of Mexico near Panama City, FL under WMO Code 1 and 2 wave conditions (World Meteorological Organization, 2014). Nominally the instrument was operated from above-ground altitudes of 15–25 m at velocities of 2–3 m/s and the laser's full beam divergence was approximately 3 mrad. For the purpose of demonstrating lidar MTF analysis, measurement timestamps were used to extract single, near-nadir swaths to reduce uncertainties that are described in Section 4.1.

3. Methods

3.1. Theoretical MTF Descriptions

MTF is evaluated using a source of signal contrast as a function of feature size or spatial frequency. For three-dimensional lidar point clouds collected from an aerial platform, a key source of measurement contrast for discerning groups of points is height, Z. The height of points across a scene is analogous to intensity across a 2-D image for which boundaries between groups of measurements can be drawn and features can be distinguished.

Not all lidar instruments record intensity along with the range measurement, but MTF can be evaluated using relative height as the source of contrast across a spatial domain. If additional sources of contrast, such as backscatter intensity, are available, MTF analysis can be applied to them to provide additional information for evaluating a system's overall MTF. The methods presented here use relative point height as the contrasting element in the MTF analysis.

Theoretical descriptions of MTF components can be estimated using properties of spatial sampling. The sampling scheme of lidar can vary among instruments, but sampling properties can be translated between camera imaging and lidar systems with comparably dense sampling patterns. The MTF methods outlined here rely on complete measurements of the PSF, which requires dense and overlapping or contiguous sampling. For lidar systems that produce sparse point clouds with no overlap between projected sample areas, the PSF will not be accurately represented by measurements with very few point source samples. Void regions, or gaps between points, observed in point clouds do not capture or illustrate the beam footprints that may have produced overlapping or contiguous samples. Beam footprints must be considered when evaluating MTF as they have a direct impact on the PSF. Therefore, it is important to highlight that these MTF methods are intended for point clouds with dense, overlapping or contiguous samples typical of "high resolution" lidar instruments.

Figure 1 illustrates an example sampling pattern for the scanning Orion lidar system where the scan rate and laser repetition rate determine the effective across-track sampling, while the effective along-track sampling is determined by the complete scan cycle rate and platform velocity. The fundamental components of MTF defined in passive imaging that are applicable to scanning lidar schemes represented by Figure 1 are the footprint and sampling MTFs in the along- and across-track axes (Boreman, 2001). In imaging, footprint MTF represents the resolution capability determined by the ground-projected size of pixels through the optical system's focal length. The equivalent footprint MTF in lidar is the ground-projected laser spot size determined by the angular beam divergence of the transmitted beam and the range to the ground, also called the instantaneous field-of-view (IFOV). Sampling MTF in imaging is representative of effective sample spacing determined by the ground-projected pixel pitch distance and in lidar it is defined by the distance between the centers of two adjacent ground-projected pulses. The equation for these MTFs as a function of spatial frequency are both represented by:

$$MTF(\xi) = |sinc(\xi x)| = \left|\frac{\sin(\pi\xi x)}{\pi\xi x}\right| \tag{6}$$

where x is the $1/e^2$ full beam width of the projected spot when evaluating footprint MTF or the ground sample distance between projected spot centers when evaluating sampling MTF (Boreman, 2001). These sinc functions represent 1-D functions for the along- and across-track axes that can be derived individually and combined to describe the 2-D sampling pattern.

These fundamental components of MTF are typically identical between the along- and across-track axes in camera imaging due to square pixels with pixel pitch ≈ pixel width (Schott, 2007; Smith, 2008). However, the sampling mechanism illustrated in Figure 1 demonstrates that the along- and across-track components of sampling can have different extents depending on mirror rotation rate, platform velocity, etc. Therefore, theoretical along-track sampling and footprint MTFs should be defined separately from the across-track counterparts using knowledge of the lidar's effective sampling parameters. Figure 2 demonstrates the difference between the axial footprint and sampling MTF components derived theoretically for the along and across track axes. The overall system MTF is defined by the combination of fundamental MTF components that impact the effective instrument spatial resolution and is commonly referred to as the cascading property of MTF (Boreman, 2001; Schott, 2007). An example of a theoretical system MTF consisting of only along- and across-track sampling and footprint MTFs is shown in Figure 2, where it can be deduced that the across-track sampling is the limiting resolution component for 3-D imaging using this ideal instrument. An example noise equivalent modulation (NEM) threshold is drawn, where the minimum detectable modulation corresponds to the intersection between NEM and MTF for quantitative evaluations of limiting resolution for an individual component or a complete system. NEM is described further in Section 3.4 for quantitative evaluations of noise relative to an MTF. For ideal instruments with no external influences on sampling, the lidar system MTF can be reliably estimated using these theoretical descriptions.

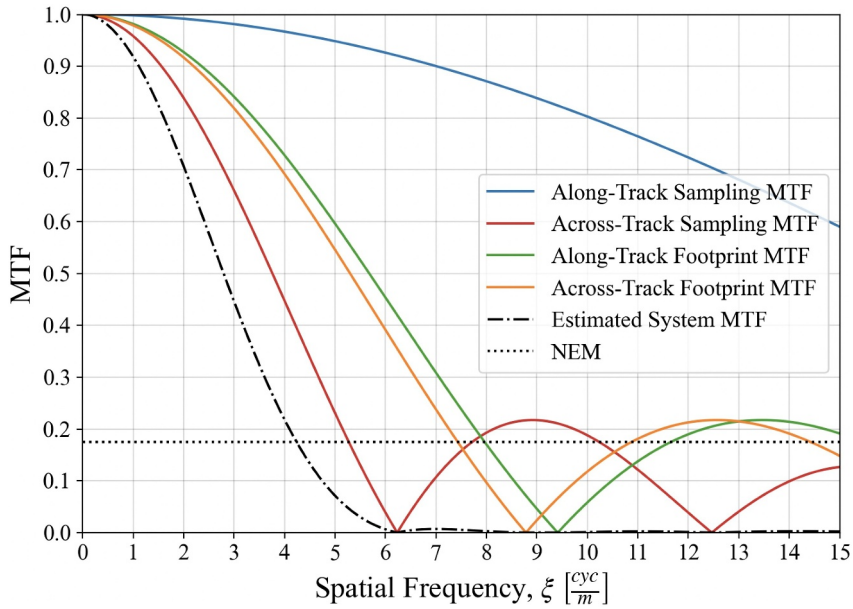

Figure 2. Theoretically-derived sampling and footprint MTFs with the estimated system modulation transfer function (MTF) for a scanning lidar instrument on an unmanned aircraft systems platform with elliptical footprints due to off-nadir scan angles. A representative noise equivalent modulation (NEM) threshold is drawn illustrating the effective cutoff frequency of the system.

Real lidar systems have a variety of measurement influences due to intrinsic noise sources, platform perturbations, and external media for which their respective MTF components, not represented in Figure 2, impact resolution and can be difficult to derive theoretically. However, through robust instrument simulations, the unknown or unquantified components of MTF that correspond to errors and uncertainties can be obtained and quantified. The simulated bathymetric point cloud shown in Figure 3 was created for the evaluation of the system MTF from theoretical principles for the lidar instrument described in Section 2, a nominal operations parameter set, and a realistic bathymetric environment. This model is built from raytracing methods where for each laser shot, several rays are traced about a pointing vector through the environment to determine the spatial envelope of the beam as a function of range. Samples are simulated as intersections between projected rays and a surface in the scene and are registered to the rays' corresponding pointing vector. Retroreflective targets can be approximated as point reflectors where the simulation registers a hit on target any time the projected beam overlaps with a target's geometry. For bathymetric simulations, the water surface steers the rays as a function of slope and as a result, the subaqueous rays are distorted, producing irregular footprints and sample-to-sample spacing. The time-variant Tessendorf water surface model described in Tessendorf (2001) is implemented to produce a dynamic water surface that can be classified to WMO standards quantitatively by wave heights and the Douglas Sea Scale or Beaufort Scale (World Meteorological Organization, 2014). Without intrinsic or extrinsic sources of uncertainty, the point cloud generated exactly matches the expected sampling map for which the footprint, sampling, and effective system MTFs are accurately represented by evaluations of Equation 6. As sources of uncertainty are introduced, any impacts on effective resolution can be quantified through MTF analysis of this synthetic data instead of basic theoretical functions.

Physical targets that produce empirical measurements of MTF through PSF and LSF analyses elucidate the total impact of MTF components without the need for complete theoretical descriptions. For active remote sensing instrumentation, point reflector targets can be used to empirically measure the OTF, or IRF, analogous to point sources in passive remote sensing applications. Corner cube retroreflectors (CCRs) have historically been used in laser applications requiring cooperative point source targets like satellite and aircraft tracking, analyzing atmospheric distortion, and georeferencing validation of lidar measurements (Lucy et al., 1966; Lutomirski & Warren, 1975; L. Magruder et al., 2005; L. A. Magruder et al., 2020). Under geometric conditions where a CCR target is sufficiently smaller than an instrument's IFOV, the three-dimensional spatial spread among lidar samples of a CCR represents the system PSF that can be used to derive MTF (Stevens et al., 2011). Similarly, linear targets that

10.1029/2024EA004098

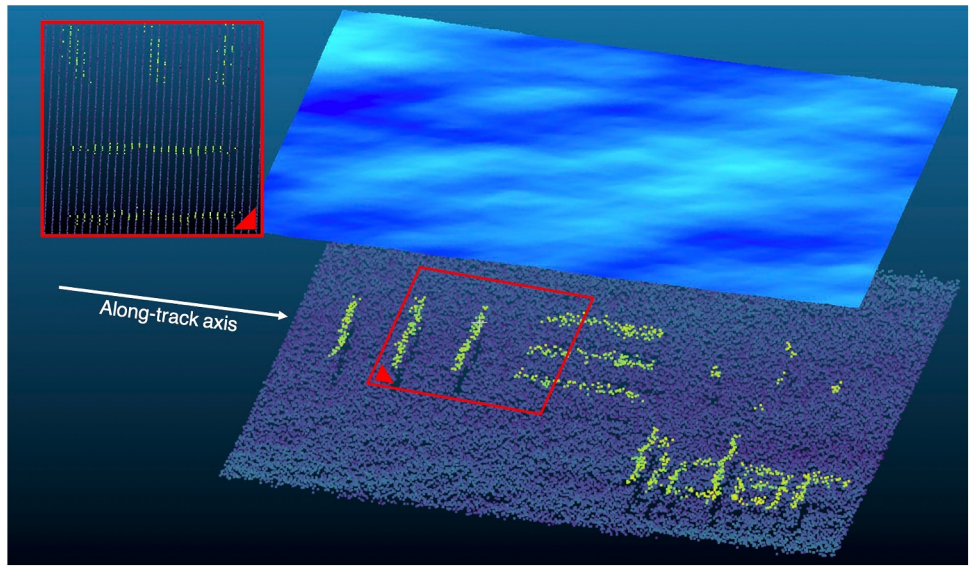

Figure 3. 3-D bathymetric lidar point cloud generated from an instrument sampling model, representative of the Orion Space Solutions system, and time-variant Tessendorf water surface model covering an area of approximately 100 m^2. The average wave height of the water surface simulated here is approx. 8 cm and classified as WMO Sea State 1 by Beaufort scale number or Douglas Sea Scale. Several 10 mm × 2 m line source targets and 50 mm diameter point source targets with simulated reflective properties are placed in the scene 30 cm above the bathymetric surface at 3 m depth for use in robust, theoretical assessment of MTF. Inset image is keyed for reorientation and shows a top-down view of the outlined region of the point cloud (a 3 × 3 m area), illustrating the dense sampling pattern produced by the simulated instrument across several linear targets.

satisfy point source conditions, that is, narrow widths and demonstrate retroreflective properties that maximize detectability, can be used to empirically measure LSF. For scanning lidar systems with sampling like Figure 1, LSF-derived MTF is a more informative metric because the measured system MTF can be decomposed to individually assess along- and across-track resolution performance. The axial components of MTF empirically measured using LSF can be directly compared to theoretical MTFs derived using Equation 6, while PSF-derived MTFs incorporate both along- and across-track sampling effects and is therefore comparable to system MTF.

3.2. Point- and Line-Reflector Target Descriptions

The point- and line-reflector targets shown in Figure 4 are used to measure PSFs and axial LSFs respectively for a UAS-based scanning topobathy lidar where the contrasting signal used for MTF analysis is height. These targets

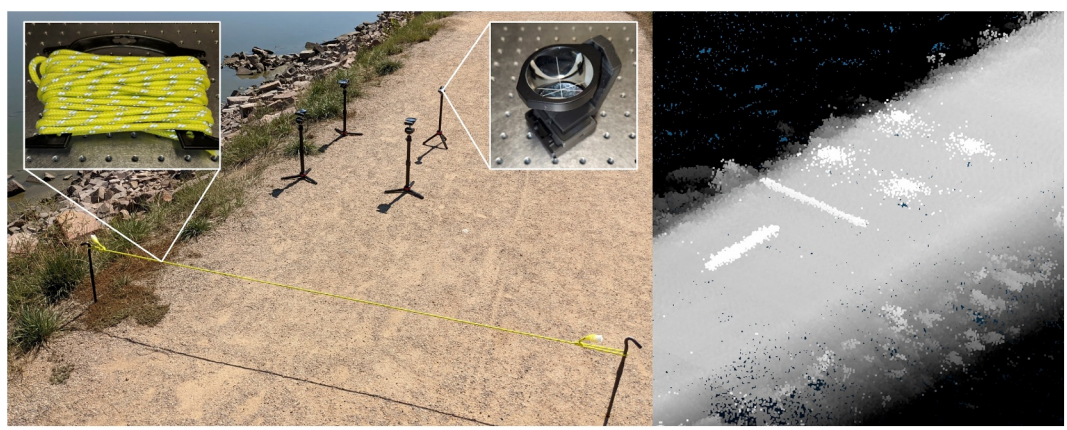

Figure 4. Image of retroreflector-woven rope line source targets and corner cube retroreflector (CCR) point source targets positioned above a level ground surface (left) and the corresponding 3-D lidar point cloud containing the targets shaded by height (right). Image cutouts depict close-up photographs of the retroreflector targets.

were selected with topographic and bathymetric lidar applications in mind due to their extremely high backscatter efficiencies, compact form factor, and capability to estimate MTF above and below a water surface. One important aspect to consider when selecting a bathymetric CCR is the method of retroreflection. Many commercially available CCRs rely on total internal reflection (TIR) as opposed to specular reflection off mirrored facets to produce retroreflection. However, it can be proven that the critical angle required for TIR-based retroreflection is not always achieved for a glass-water interface depending on the dimensions or the refractive index of the CCR (Hecht, 2017). The 50 mm diameter CCR targets used here and shown in Figure 4 are silver-plated to produce retroreflection when underwater and the outside substrates have been epoxy-coated to protect the mirrored surface from degradation.

The lidar system used for demonstrating MTF produces dense sampling maps with overlapping spots in the along-track axis. From 15 m altitude, the estimated nadir footprint diameter is 65 mm, with 24 and 90 mm along- and across-track sample distances respectively. From 25 m altitude, expected nadir footprint diameters are 110 mm, with 24 and 150 mm along- and across-track sample distances respectively. These estimates indicate strong overlap in the along-track but not in the across-track. The 50 mm CCRs were sized to ensure target "hits" at nadir in the across-track axis for these sample distance and footprint estimates where smaller CCRs could result in "misses". Smaller CCRs satisfy geometric point source conditions more easily, but larger CCRs also increase detectability in bathymetric surveys. Therefore, the largest CCRs that adequately approximate point source conditions for this demonstration instrument were selected. Additionally, any PSF errors originating from poor point source approximations can be quantified and compensated using convolution analysis for two finite-area sources (Gaskill, 1978).

For LSF analysis, the 8 mm diameter, 2 m long retroreflective rope shown in Figure 4 is deployed horizontally level and suspended above the ground using stakes or screw anchors. The 8 mm diameter easily satisfies geometric point source conditions, but in this case, occasional "misses" do not impact the LSF result. Due to the extended length of the LSF target, a sufficient number of samples are produced (see Figures 5 and 6) such that any impacts to the LSF due to "misses" are effectively negated. The reflective filament woven throughout the rope consists of retroreflective microspheres that function underwater. LSF-based MTF analysis offers added utility over PSF analysis for discerning along-track and across-track system effects. These retroreflective targets maximize the likelihood of detection within the effective IFOV (see Figure 1) as point and line sources, making them ideal targets for empirical MTF analysis of lidar instruments. The Geiger-mode lidar instrument used is resilient against saturation effects that can make retroreflective materials challenging to use with other types of lidar instruments. Other instruments can still leverage retroreflectors but relevant detector sensitivities that would determine maximum target size or minimum separation distance should be considered.

3.3. Empirical PSF- and LSF-Derived MTFs

Figure 5a illustrates a topographic region of interest (ROI) around a line-reflector target suspended 30 cm above a flat surface (shown in Figure 4) to isolate the two signal sources used to estimate MTF from the LSF. In this example, the instrument's across-track axis is defined as X, the along-track axis as Y, and the vertical axis as Z. The accompanying Z histogram in Figure 5b shows a clear discernibility between points corresponding to the line target and those associated with the ground. A line is fit to the points corresponding only to the linear target, then 3-D affine transformations are applied to the ROI point cloud to align the line fit orthogonal to the X-Z plane to minimize the line spread, as shown in Figure 6a. It is important to configure the line target to be parallel to the flat background surface to minimize the X-Z spread of the background. With the Y-axis effectively removed, this 2-D point cloud is then interpolated along the X-axis with fine sampling (example shown in Figure 6a uses 1 mm sampling) to produce a supersampled LSF, analogous to the LSFs used for MTF analysis in imaging using the slant-edge MTF method (Burns, 2000). Like the slant-edge MTF method, a low-pass Tukey filter is applied to the normalized LSF to effectively smooth out MTFs from discontinuities caused by high frequency noise (Burns et al., 2022). In the example shown in Figure 6b, $\alpha = 0.8$ is used to preserve the existing LSF features whereas an equivalent Hann filter ($\alpha = 1.0$) would narrow the LSF and artificially boost the resulting MTF in a way that is not representative of the lidar system. MTF is obtained by taking the Fourier transform of the Tukey-filtered, normalized LSF with many examples shown in Section 4.

The process to obtain a PSF-derived MTF using a CCR target is nearly identical to the LSF-based method and the primary difference is how the 3-D point cloud is transformed into the X-Z plane. Instead of a line fit, a centroid is

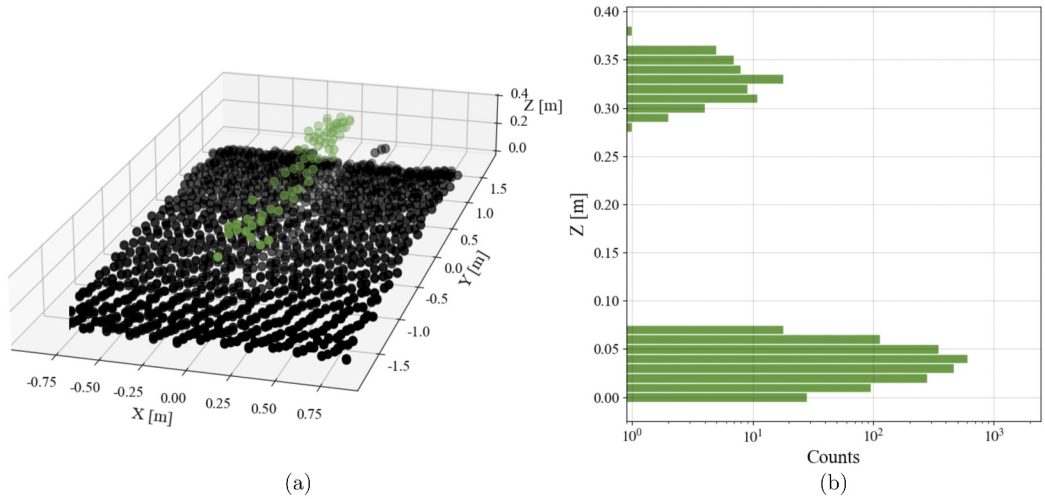

Figure 5. (a) 3-D lidar point cloud of line target sampled from a UAS platform. (b) The corresponding histogram as a function of height, demonstrating clear contrast between target and background. Measurements in green correspond to the target while black points correspond to the background beneath the target. The line target in this example is oriented parallel to the path of motion, therefore the spread of points in the point cloud is indicative of the across-track resolution performance of the lidar instrument system.

fit to the 3-D distribution of points corresponding to the CCR target and is set as the origin of the *X*-*Y* plane. Points within the resulting Cartesian quadrants I and III are rotated about the centroid *Z*-axis clockwise, maintaining their radial centroid distance, into the *X*-*Z* plane, while points within quadrants II and IV are rotated counter-clockwise into the *X*-*Z* plane. Due to this rotation of the along-track spread into the across-track axis, the PSF-derived MTF is closer in theory to the system MTF line illustrated in Figure 2. The resulting 2-D point cloud resembles Figure 6a and subsequent processing is identical to the LSF MTF method to obtain a PSF-derived MTF.

3.4. Quantitative Evaluation of MTF

Evaluating MTF quantitatively is helpful for deriving metrics that relate MTF to physical dimensions or for comparing resolution performance between different instruments using metrics other than limiting resolution. The limiting resolution of the instrument is commonly determined using a constant modulation transfer threshold (often 5%, 10%, or 20%) in imaging and in previous applications of CTF to lidar (Holst, 2008; Lichti, 2004;

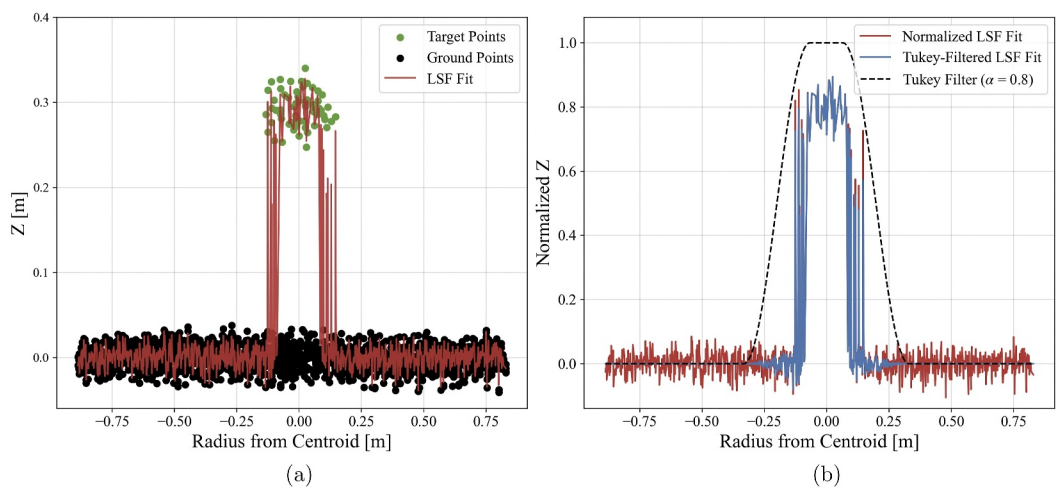

Figure 6. *X*-*Z* view of 3-D lidar point cloud shown in Figure 5a with a line spread function (LSF) fit (a) and the corresponding normalized, Tukey-filtered LSF used to compute MTF (b). This Tukey filter was configured using $\alpha = 0.8$ to prevent artificial narrowing of the LSF. An offset in Z was applied to the point cloud from Figure 5 to produce a zero-mean background.

Stevens et al., 2011). However, constant thresholds like these are subjectively determined and do not sufficiently describe noise or meaningfully compare instruments. A quantitative method for determining the limiting resolution is deriving an instrument system's NEM threshold, also called minimum detectable modulation (Boreman, 2001). NEM captures the cumulative impact from noise and systematic effects that impact effective contrast, which for height-based MTF analysis represents the minimum vertical relief required to reliably discern an object from its surroundings. Additionally, due to the relationship between lidar's range-time measurement mode and the vertical coordinate of measurements used as the source of contrast for MTF, the IRF is a component of NEM. NEM can be illustrated using histograms like Figure 5b or PSF/LSF plots like Figure 6a where the spread in the Z-axis around objects that act as Dirac delta functions in range-time, such as a suspended line target or a level surface, demonstrate an effective signal-to-noise ratio (SNR) related to M and NEM.

$$SNR = \frac{M}{NEM} \tag{7}$$

where for normalized LSFs, $M \approx 1$ such that:

$$NEM = \frac{1}{SNR} = \frac{N}{S} \tag{8}$$

where N is the noise, or the random spread in Z values, defined here as the full width at half maximum of the background histogram in Z, and S is the mean signal, defined here as the mean difference in Z between the target and background. The limiting resolution is equal to one half-cycle of the cutoff frequency found at the intersection of MTF and NEM, or:

$$d = \frac{\lambda}{2} = \frac{1}{2f} \tag{9}$$

where d is the limiting target width and f is the cutoff frequency (Schott, 2007).

4. Results

4.1. Topographic MTF

The along-track resolution of the UAS platform topobathy lidar instrument system described in Section 2 was evaluated through the sampling of a line source target oriented perpendicular to the flight axis (opposite to Figure 5) to produce the empirical MTF shown in Figure 7 representing along-track resolution performance. The theoretical MTF was estimated using the product of fundamental footprint and sampling MTFs obtained using Equation 6 for the along-track axis components only. In this result, the strong agreement between empirical and theoretical MTFs demonstrates that these fundamental components of MTF provide a close estimate of true along-track resolution performance for topographic targets. Evaluating MTF using the empirically-derived NEM threshold suggests a limiting spatial frequency of approximately 8.75 cycles per meter, or a limiting resolution of 5.71 cm using Equation 9 to invert spatial frequency into an equivalent target diameter.

The across-track resolution of the system was evaluated using a line source target oriented parallel to the flight axis, represented by Figure 5, producing the empirical MTF shown in Figure 8. However, in this case the same theoretical description of MTF used to evaluate along-track performance does not agree well with the empirical measurements in the across-track axis. This is an indication that there are additional components of MTF not captured by the theoretical estimate using only footprint and sampling MTFs. Because the lidar's scan axis is aligned in the across-track axis of flight, scan angle pointing uncertainties have a greater impact in the across-track axis than the along-track axis in terms of effective point spread or line spread. Therefore, the lidar measurement simulation tool described in Section 3.1 was used to reproduce expected sampling patterns for which pointing uncertainties could also be introduced. The simulation used a retroreflective line source target and identical flight and sampling parameters to generate a point cloud for which an augmented theoretical MTF could be evaluated and compared to the empirical MTF. A random error was applied to the pointing vector prior to raytracing each laser shot to simulate pointing uncertainty and its impact on MTF. Monte Carlo simulations ($N = 500$) that varied the mean pointing error were generated, from which a pointing error of approximately $\pm 0.2°$

10.1029/2024EA004098

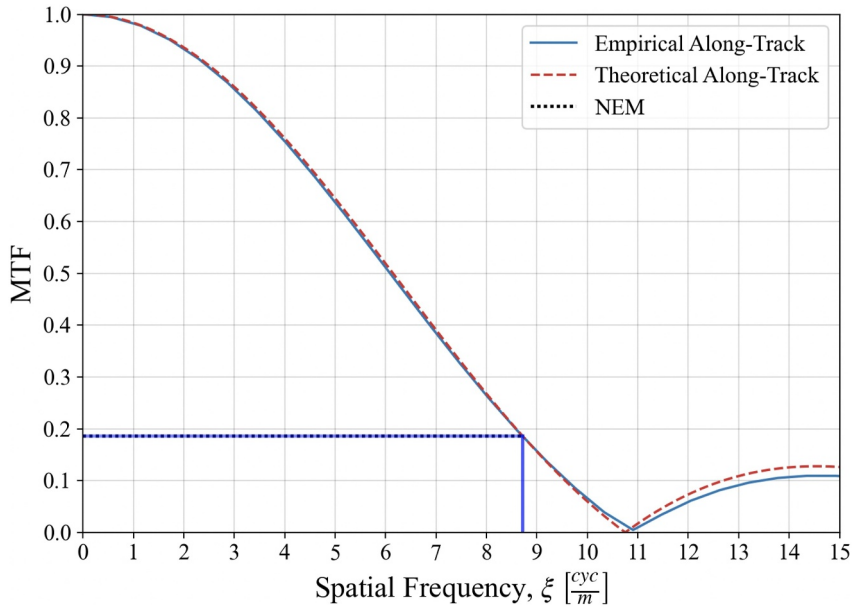

Figure 7. Empirical and theoretical LSF-derived MTFs evaluated in the along-track axis for a target oriented perpendicular to the flight path (opposite to Figure 5). The intersection of the MTF curve and the NEM threshold corresponds to the minimum detectable modulation of the system to determine the limiting resolution.

was found to minimize the difference between MTFs obtained from simulated data and the empirical MTF shown in Figure 8. Additional sources of instrument or platform error may be contributing to the observed ±0.2 degrees of error, but the axial dependence of this error leads to the conclusion that pointing error is the dominant source of error. Consultation with the manufacturer Orion Space Solutions confirmed this level of pointing uncertainty for this instrument.

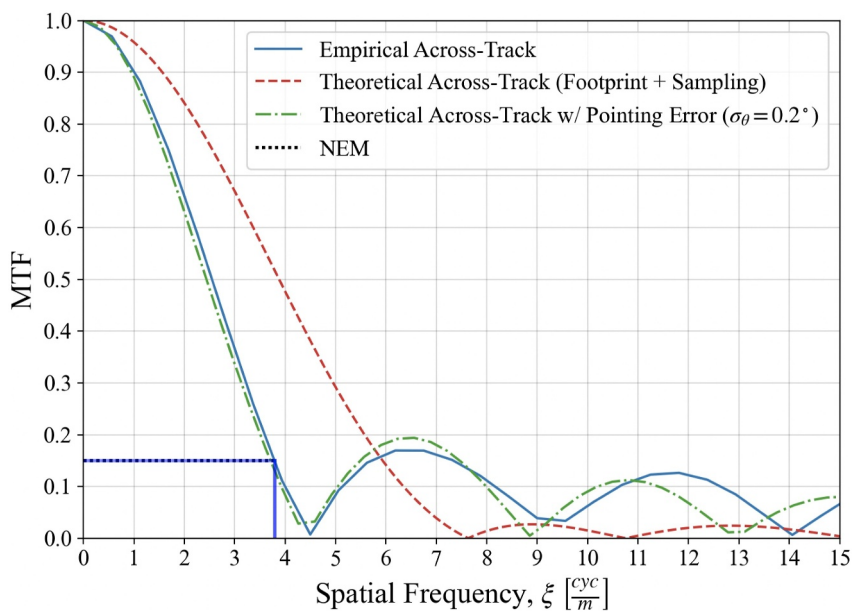

Figure 8. Empirical and theoretical LSF-derived MTFs evaluated in the across-track axis for a target oriented parallel to the flight path. The empirical MTF plotted corresponds to the point cloud and LSFs shown in Figures 5 and 6. Simulated point cloud data was used to enable models of instrument pointing error as an additional component of MTF. The augmented theoretical model with an instrument pointing error of ±0.2° in the across-track axis produces an MTF estimate that strongly aligns with empirical MTF results.

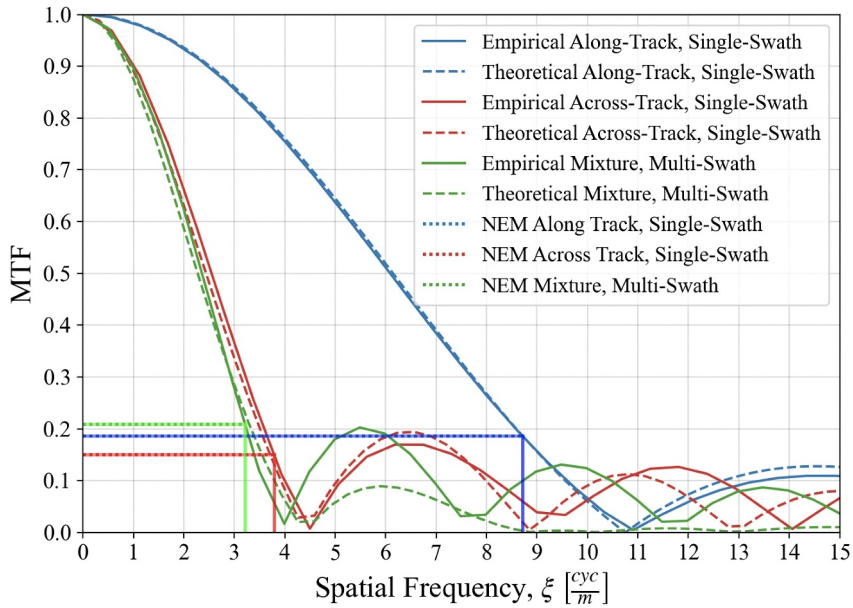

Figure 9. Empirical and theoretical MTFs for point clouds collected using single swaths over a line target and a point cloud collected using multiple swaths comprised of a mixture of flight path orientations with respect to the axis of the line target. NEM thresholds are derived empirically from the point cloud data used for MTF analysis to evaluate their respective MTFs.

Evaluating the across-track MTF using NEM suggests a limiting spatial frequency of approximately 3.80 cycles per meter, or an equivalent resolution limit of 13.2 cm for the across-track axis of the instrument. Comparing across-track to along-track performance, these empirical and theoretical MTF results demonstrate the poorest resolution in the instrument system is the effective across-track sampling. This is due to the nominal ground sample distances produced by the scanning configuration and the pointing uncertainties in the scan axis, which is likely caused by measurement errors in mirror angle position or platform orientation determined by the instrument's inertial measurement unit.

Figure 9 compares empirical and theoretical MTFs between perpendicular single-swath and multi-swath point clouds containing a line target. The single-swath, along- and across-track MTFs bound the spectrum of single-swath MTFs for line targets with arbitrary orientation angles relative to the flight axis. However, for multi-swath point clouds, due to the cascading nature of MTF, it is expected that mixtures of along-track, across-track, and other effects stack on the overall result, producing an effectively lower system resolution (Boreman, 2001; Schott, 2007; Smith, 2008). This predictable behavior is observed in Figure 9, for both the empirical and simulated theoretical MTFs for multi-pass mixtures of different flight angles with respect to the target axis. The blending of along- and across-track sampling effects into a single MTF result is also a characteristic of PSF-derived MTFs for which each axial component contributes to the overall spread of a point source target. This is also similar to a system MTF which is the product of each component of MTF present in the end-to-end system description.

Aggregating multiple swaths' point clouds introduces additional components of MTF that impact resolution performance and can often be neglected in short, single-swath analyses. Single swaths using this demonstration instrument produced sufficient target samples for these LSF MTF results due to the extended length of the target. However, for PSF MTF analyses where single swaths do not produce sufficient target samples, aggregating multiple swaths is necessary to completely describe the PSF. Sources of uncertainty that impact point georeferencing processes, such as GPS drift errors that vary over time or boresighting errors that vary with flight heading, are potential sources of additional point or line spread that effectively decrease the overall system MTF (Stevens et al., 2011; Thayer et al., 2022). Depending on the lidar system, sources of uncertainty such as these could introduce meaningful or negligible components of MTF as part of the complete instrument system MTF description. In the example shown in Figure 9, the augmented theoretical description of MTF for a multi-swath point cloud aligns strongly with the empirical MTF without modeling sources of error like GPS drift or boresight

errors in the theoretical description, implying these error components of MTF are of low impact. However, for systems with extremely high-resolution capability these sources of error may have measurable impact on the resolution limit and could be interrogated through MTF methods.

4.2. Bathymetric MTF

Figure 10 demonstrates that MTF can also be used to quantify unknown environmental impacts on effective resolution, such as the dynamic water surface and column effects for bathymetric lidar applications. In the example shown by Figure 10a, PSF-derived MTF was calculated using multiple aggregated swaths of topobathymetric point clouds containing measurements of one CCR target deployed on a beach and another CCR target deployed to a depth of 3 m offshore. Multiple swaths were needed to produce sufficient samples of the PSF for MTF evaluation. The theoretical description of MTF aligns strongly with the empirical MTF corresponding to the topographic CCR, as found in Figures 8 and 9.

Figure 10b illustrates that the same theoretical MTF description used for the topographic CCR, when applied to the bathymetric CCR, results in a misalignment between theoretical and empirical MTFs. This suggests a similar situation as the across-track LSF topographic MTF example in Figure 8 where the known components of MTF do not adequately describe the empirical results, and in this case is due to the intervening water medium. The water surface introduces additional steering errors and pulse stretching caused by wave slopes resulting in optical path length and direction uncertainties, while the water column introduces beam spread through forward scattering processes, resulting in larger projected spot sizes (Measures, 1984; Mobley, 1995). These errors introduce three-dimensional point spread that impact MTF. The increased spread in the X-Y plane increases the PSF width, effectively decreasing the MTF width, while the increased spread in the Z-axis corresponds to higher levels of NEM, shown in Figure 10b, resulting in reduced resolution limits as effective contrast in Z is reduced.

In addition to the augmented theoretical MTF description that includes instrument pointing errors, simulated point cloud data was enhanced further using the Tessendorf water surface model (Tessendorf, 2001). This model provided surface waves whose variation in slopes produced steering errors in both the along- and across-track axes in the simulated point cloud. Minimizing the difference between empirical and theoretical MTFs generated using Monte Carlo simulations ($N = 100$), a steering error of $\pm 6.0°$ was determined to best-represent the overall effects by the water on MTF. As previously mentioned, water surface steering errors are not the only component of MTF introduced by the water. However, these results demonstrate that further augmentations to the theoretical description of MTF using simulated lidar point cloud data can encapsulate the overall extent of effects caused by external sources of unknown severity. Applying known physical processes to those sources, the resulting theoretical MTF agrees well with the empirical MTF. Therefore, empirical MTF analyses can also be

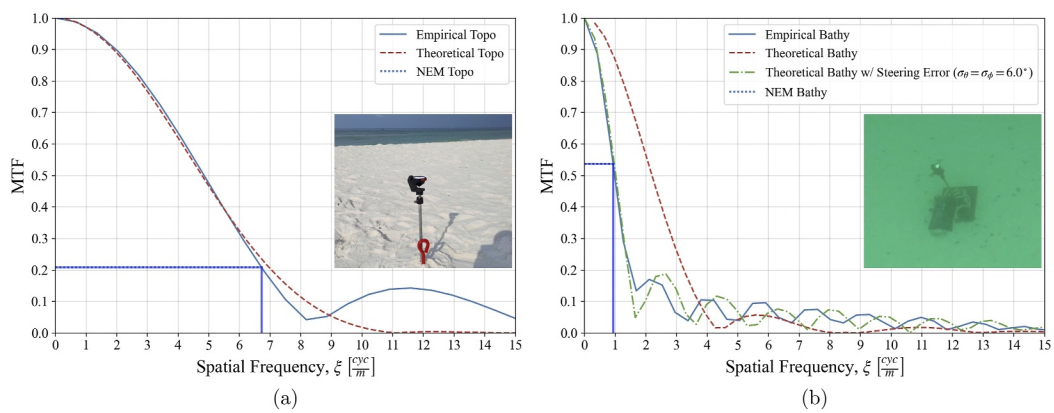

Figure 10. (a) Empirical and theoretical topographic MTFs for a CCR target set up on the beach where the theoretical MTF model is the same as Figures 8 and 9. (b) Empirical and theoretical bathymetric MTFs for a CCR target submerged to 3 m depth offshore. Image inserts show the CCR targets in their respective deployments. The theoretical bathy MTF was augmented with simulated point cloud data to estimate steering error of subaqueous optical paths through rough water surfaces. An augmented theoretical bathy MTF using ±6.0 degrees of water surface steering errors in both the across- and along-track axes aligns with empirical MTF results.

performed to reliably capture and quantify the impacts on resolution from unknown environmental influences as well as known instrument system properties.

5. Conclusions

Theoretical and empirical MTFs have been shown to strongly agree using MTF methods commonly applied in passive camera imaging applications that have been adapted for lidar measurement modes. Through demonstrations using height as the contrasting signal across a three-dimensional point cloud scene generated by a UAS-based topobathy lidar, MTF analysis has quantified instrumental and environmental sampling behaviors and, more broadly, demonstrates that MTF analysis can serve as a robust means for evaluating resolution performance for any lidar mapping system. While PSF-derived MTFs provided an overall evaluation of resolution combining along- and across-track instrument effects, LSF-derived MTFs enabled the axial decomposition of MTF to separately describe the along- and across-track characteristics for the scanning lidar system employed in this study. Components of MTF previously missing from theoretical descriptions were identified and incorporated into model simulations resulting in augmented theoretical MTFs that strongly aligned with empirical MTFs determined from compact calibration targets. Unknown intrinsic pointing errors in the across-track axis were quantified using robust point cloud simulation tools to produce synthetic MTFs that match empirically-derived MTFs, shown in Figures 8 and 9. A similar approach was taken to quantify the extrinsic beam steering uncertainties by a rough water surface that influenced resolvability in bathymetric scenes, shown in Figure 10. MTF's ability to quantify intrinsic and extrinsic influences on resolution strongly supports the adoption of MTF as a standard in hydrographic surveying and other high resolution bathymetry applications that do not have standardized empirical methods for quantifying resolution.

Previous applications of MTF in lidar mainly involved using very large tribar targets that indirectly captured MTF through empirically derived measures of CTF (Miles et al., 2010; Stevens et al., 2011). Direct measurements of MTF through PSF and LSF methods utilizing edge, line, and point source targets have extensive heritage in passive camera imaging and has been successfully applied here to a scanning topobathy lidar. Additionally, these compact targets can be easily acquired, transported, and deployed for standardized use in high resolution lidar surveys to add resolution validation, ground control points, and georeferencing validation capabilities to post-processing pipelines (L. A. Magruder et al., 2020). While ESF-based lidar MTFs have been demonstrated by Goesele et al. (2003), dynamic bathymetric environments inhibit the feasibility of edge source targets compared to compact point and line sources. Retroreflective sources maximize the detectability of MTF targets making them ideal for robust estimation of effective resolution in bathymetric lidar applications where unknown environmental factors can cause large departures from theoretical representations of resolution capability. These targets enabled the empirical estimation of water surface slopes in shallow waters, adding context to measurements with otherwise unknown environmental information. Additionally, deploying a series of bathymetric MTF targets at known depths enables direct measures of effective spatial resolution as a function of depth, which can greatly inform bathymetric applications such as underwater target detection and classification (Sacca & Thayer, 2023).

MTF represents a unifying metric for resolution validation of camera imaging and lidar instruments alike, enabling direct performance comparisons and providing empirical references of resolution for data fusion applications. Large-scale surveys utilizing a suite of instrumentation, such as NASA's STV program, can leverage MTF as a common metric to calibrate lidar and camera measurements collected at different times and across various platforms or environmental conditions. Standardizing the utility of MTF to lidar will improve the quality and potential of point cloud analysis and data science with empirical evidence of effective resolution to support theoretical resolution estimates. These MTF methods can also be extended to include lidar instrument systems that record radiometric intensity of backscattered pulses, combining the use of height and intensity as contrasting signal sources to perform multi-modal MTF analysis.

Data Availability Statement

Lidar point cloud data supplied by Orion Space Solutions (2025) were used in the production of this manuscript. The subsets of empirical topographic and bathymetric point cloud data used in the presented MTF analyses and the processing software used to generate the presented figures are available under the MIT license from GitHub at

https://github.com/UCBoulder/3DMTF (Sacca, 2024). Matplotlib version 3.7.3 (Caswell et al., 2023; Hunter, 2007) was used to create figures and is available under the Matplotlib license at https://matplotlib.org.

Acknowledgments
This research was partially supported by NASA FINESST Grant Number 80NSSC21K1597. UAS-based lidar data was collected in collaboration with Orion Space Solutions, Louisville, CO 80027 USA. This work was also supported in part by the U.S. Department of Defense, through the Strategic Environmental Research and Development Program (SERDP-ESTCP, 2024) Contract Number W912HQ22C0042. Views, opinions, and/or findings contained in this report are those of the authors and should not be construed as an official Department of Defense position or decision unless so designated by other official documentation.

References

Albota, M., Gurjar, R., Mangognia, A., Dumanis, D., & Edwards, B. (2017). The airborne optical systems testbed (AOSTB). In *Military sensing symp*.

Boreman, G. D. (2001). *Modulation transfer function in optical and electro-optical systems* (Vol. 4). SPIE press. https://doi.org/10.1117/3.419857

Boreman, G. D., & Yang, S. (1995). Modulation transfer function measurement using three-and four-bar targets. *Applied Optics*, *34*(34), 8050–8052. https://doi.org/10.1364/ao.34.008050

Burns, P. D. (2000). Slanted-edge mtf for digital camera and scanner analysis. In *Proc. IST 2000 PICS conference* (pp. 135–138).

Burns, P. D., Masaoka, K., Parulski, K., & Wueller, D. (2022). Updated camera spatial frequency response for iso 12233. *Electronic Imaging*, *34*(9), 1–6. https://doi.org/10.2352/ei.2022.34.9.iqsp-357

Caswell, T., Droettboom, M., Lee, A., Hunter, J., Firing, E., Stansby, D., et al. (2023). Matplotlib v3.7.3 [Software]. *Matplotlib v3.7.3* https://doi.org/10.5281/zenodo.8336761

Collin, A., Archambault, P., & Long, B. (2008). Mapping the shallow water seabed habitat with the shoals. *IEEE Transactions on Geoscience and Remote Sensing*, *46*(10), 2947–2955. https://doi.org/10.1109/tgrs.2008.920020

Coltman, J. W. (1954). The specification of imaging properties by response to a sine wave input. *JOSA*, *44*(6), 468–471. https://doi.org/10.1364/josa.44.000468

Dolin, L. S. (2013). Theory of lidar method for measurement of the modulation transfer function of water layers. *Applied Optics*, *52*(2), 199–207. https://doi.org/10.1364/ao.52.000199

Donnellan, A., Glennie, C., Green, J., Stephen, M., Lundgren, P., Medley, B., et al. (2024). Nasa's surface topography and vegetation study. In *Igarss 2024 - 2024 ieee international geoscience and remote sensing symposium* (pp. 2259–2261). https://doi.org/10.1109/IGARSS53475.2024.10641876

Donnellan, A., Harding, D., Lundgren, P., Wessels, K., Gardner, A., Simard, M., et al. (2021). Observing earth's changing surface topography and vegetation structure: A framework for the decade. *NASA surface topography and vegetation incubation study*, *210*.

Eon, R., Wenny, B. N., Poole, E., Eftekharzadeh Kay, S., Montanaro, M., Gerace, A., & Thome, K. J. (2024). Landsat 9 thermal infrared sensor-2 (tirs-2) pre-and post-launch spatial response performance. *Remote Sensing*, *16*(6), 1065. https://doi.org/10.3390/rs16061065

Fiete, R. D. (1999). Image quality and [lambda] fn/p for remote sensing systems. *Optical Engineering*, *38*(7), 1229–1240. https://doi.org/10.1117/1.602169

Forfinski-Sarkozi, N. A., & Parrish, C. E. (2019). Active-passive spaceborne data fusion for mapping nearshore bathymetry. *Photogrammetric Engineering and Remote Sensing*, *85*(4), 281–295. https://doi.org/10.14358/pers.85.4.281

Gaskill, J. D. (1978). *Linear systems, fourier transforms, and optics* (Vol. 56). John Wiley and Sons.

Goesele, M., Fuchs, C., & Seidel, H.-P. (2003). Accuracy of 3d range scanners by measurement of the slanted edge modulation transfer function. In *Fourth international conference on 3-d digital imaging and modeling, 2003. 3dim 2003. proceedings* (pp. 37–44).

Goulden, T., & Hopkinson, C. (2010). The forward propagation of integrated system component errors within airborne lidar data. *Photogrammetric Engineering and Remote Sensing*, *76*(5), 589–601. https://doi.org/10.14358/pers.76.5.589

Hancock, S., Armston, J., Hofton, M., Sun, X., Tang, H., Duncanson, L. I., et al. (2019). The gedi simulator: A large-footprint waveform lidar simulator for calibration and validation of spaceborne missions. *Earth and Space Science*, *6*(2), 294–310. https://doi.org/10.1029/2018ea000506

Hecht, E. (2017). *Optics* (5ed ed.). Pearson Education, Inc.

Holst, G. C. (2008). *Electro-optical imaging system performance* (5th ed.). SPIE- International Society for Optical Engineering.

Hunter, J. D. (2007). Matplotlib: A 2d graphics environment. *Computing in Science & Engineering*, *9*(03), 90–95. https://doi.org/10.1109/mcse.2007.55

International Hydrographic Organization. (2022). Standards for hydrographic surveys. S-44 Edition 6.1.0.

Kellner, J. R., Armston, J., Birrer, M., Cushman, K., Duncanson, L., Eck, C., et al. (2019). New opportunities for forest remote sensing through ultra-high-density drone lidar. *Surveys in Geophysics*, *40*(4), 959–977. https://doi.org/10.1007/s10712-019-09529-9

Kuester, M. A., Johnson, B. R., Kampe, T. U., & McCorkel, J. (2010). Calibration system stability plans for a long-term ecological airborne remote sensing project. In *2010 ieee international geoscience and remote sensing symposium* (pp. 593–595).

Lichti, D. D. (2004). A resolution measure for terrestrial laser scanners. International Archives of Photogrammetry. *Remote Sensing and Spatial Information Sciences*, *34*(34), B5.

Lucy, R., Peters, C., McGann, E., & Lang, K. (1966). Precision laser automatic tracking system. *Applied Optics*, *5*(4), 517–524. https://doi.org/10.1364/ao.5.000517

Lutomirski, R. F., & Warren, R. E. (1975). Atmospheric distortions in a retroreflected laser signal. *Applied Optics*, *14*(4), 840–846. https://doi.org/10.1364/ao.14.000840

Magruder, L., Silverberg, E., Webb, C., & Schutz, B. (2005). In situ timing and pointing verification of the icesat altimeter using a ground-based system. *Geophysical Research Letters*, *32*(21), L21S04. https://doi.org/10.1029/2005gl023504

Magruder, L. A., Brunt, K. M., & Alonzo, M. (2020). Early icesat-2 on-orbit geolocation validation using ground-based corner cube retroreflectors. *Remote Sensing*, *12*(21), 3653. https://doi.org/10.3390/rs12213653

Mandlburger, G. (2022). A review of active and passive optical methods in hydrography. *International Hydrographic Review*, *28*, 8–52. https://doi.org/10.58440/ihr-28-a15

Mandlburger, G., Pfennigbauer, M., Schwarz, R., Flöry, S., & Nussbaumer, L. (2020). Concept and performance evaluation of a novel uav-borne topo-bathymetric lidar sensor. *Remote Sensing*, *12*(6), 986. https://doi.org/10.3390/rs12060986

Markham, B. L. (1985). The landsat sensors' spatial responses. *IEEE Transactions on Geoscience and Remote Sensing*(6), 864–875. https://doi.org/10.1109/tgrs.1985.289472

McCarthy, M. J., Otis, D. B., Hughes, D., & Muller-Karger, F. E. (2022). Automated high-resolution satellite-derived coastal bathymetry mapping. *International Journal of Applied Earth Observation and Geoinformation*, *107*, 102693. https://doi.org/10.1016/j.jag.2022.102693

Measures, R. M. (1984). *Laser remote sensing: Fundamentals and applications*. Wiley-Interscience.

Miles, B. H., Kamerman, G. W., Fronek, D. K., & Eadon, P. (2010). Calibration targets and standards for 3d lidar systems. *Laser radar technology and applications xv*, *7684*, 142–151.

Miles, B. H., Land, J. E., Hoffman, A. L., Humbert, W. R., Smith, B. A., Howard, A. B., et al. (2002). Field-testing protocols for evaluation of 3d imaging focal plane array ladar systems. *Laser radar technology and applications vii*, *4723*, 43–56. https://doi.org/10.1117/12.476413

Mobley, C. D. (1995). The optical properties of water. *Handbook of optics*, *1*(43), 43.

National Oceanic and Atmospheric Administration. (2020). *Field procedures manual*. Office of Coast Survey: Hydrographic Surveys Division.

Orion Space Solutions. (2025). Orion space Solutions. Retrieved from https://orion.arcfield.com/

Parrish, C. E., Magruder, L. A., Neuenschwander, A. L., Forfinski-Sarkozi, N., Alonzo, M., & Jasinski, M. (2019). Validation of icesat-2 atlas bathymetry and analysis of atlas's bathymetric mapping performance. *Remote Sensing*, *11*(14), 1634. https://doi.org/10.3390/rs11141634

Parrish, C. E., Rogers, J. N., & Calder, B. R. (2013). Assessment of waveform features for lidar uncertainty modeling in a coastal salt marsh environment. *IEEE Geoscience and Remote Sensing Letters*, *11*(2), 569–573. https://doi.org/10.1109/lgrs.2013.2280182

Reichenbach, S. E., Park, S. K., & Narayanswamy, R. (1991). Characterizing digital image acquisition devices. *Optical Engineering*, *30*(2), 170–177. https://doi.org/10.1117/12.55783

Sacca, K. W. (2024). 3DMTF version 1.0.0 [Software]. *3DMTF version 1.0.0*. Retrieved from https://github.com/UCBoulder/3DMTF

Sacca, K. W., & Thayer, J. P. (2023). Water column compensation using submersible calibration targets for 3d lidar bathymetry. In *Igarss 2023-2023 ieee international geoscience and remote sensing symposium* (pp. 471–474).

Schott, J. R. (2007). *Remote sensing: The image chain approach*. Oxford University Press.

Schwarz, R., Mandlburger, G., Pfennigbauer, M., & Pfeifer, N. (2019). Design and evaluation of a full-wave surface and bottom-detection algorithm for lidar bathymetry of very shallow waters. *ISPRS Journal of Photogrammetry and Remote Sensing*, *150*, 1–10. https://doi.org/10.1016/j.isprsjprs.2019.02.002

SERDP-ESTCP. (2024). Strategic environmental research and development program and the environmental security technology certification program. Retrieved from https://serdp-estcp.org/

Smith, W. J. (2008). *Modern optical engineering: The design of optical systems* (4th ed.). McGraw-Hill.

Stevens, J. R., Lopez, N. A., & Burton, R. R. (2011). Quantitative data quality metrics for 3d laser radar systems. *Laser radar technology and applications xvi*, *8037*, 167–181.

Storey, J. C. (2001). Landsat 7 on-orbit modulation transfer function estimation. *Sensors, systems, and next-generation satellites v*, *4540*, 50–61.

Tessendorf, J. (2001). Simulating ocean water. Simulating nature: Realistic and interactive techniques. *SIGGRAPH*, *1*(2), 5.

Thayer, J. P., Thompson, G., Sacca, K. W., & Wise, A. K. (2022). Investigative methods to assess a drone-based, topobathy lidar sensor for shallow-water munitions response. In *Oceans 2022, hampton roads* (pp. 1–7).

Ullrich, A., & Pfennigbauer, M. (2016). Linear lidar versus geiger-mode lidar: Impact on data properties and data quality. *Laser radar technology and applications xxi*, *9832*, 29–45.

Welsh, B. M., & Gardner, C. S. (1989). Performance analysis of adaptive-optics systems using laser guide stars and sensors. *JOSA A*, *6*(12), 1913–1923. https://doi.org/10.1364/josaa.6.001913

Williams, D., & Burns, P. D. (2001). Diagnostics for digital capture using mtf. In *Pics* (pp. 227–232).

World Meteorological Organization. (2014). Guide to meteorological instruments and methods of observation. *WMO-No. 8, 2014 edition*.